Engineering Science & Technology
https://ojs.wiserpub.com/index.php/EST/

UNIVERSAL WISER PUBLISHER

Research Article

Numerical Study of Vortex Dynamics in MVG-Controlled Hypersonic Flow at Mach 5.0

Yonghua Yan[1], Yong Yang[2], Caixia Chen[1*], Demetric I Baines[1]

[1]Department of Mathematics and Statistical Sciences, Jackson State University, Jackson, MS, 39217, USA
[2]Department of Mathematics, West Texas A&M University, Canyon, TX, 79016, USA
E-mail: caixia.chen@jsums.edu

Received: 22 April 2025; **Revised:** 26 June 2025; **Accepted:** 7 July 2025

Abstract: This study conducts a Large Eddy Simulation (LES) to investigate MVG-controlled hypersonic flow at Mach 5.0, analyzing flow structures such as momentum deficits and coherent vortex formations. Comparisons with Mach 2.5 flow reveal that increasing the Mach number makes ring-like vortices harder to distinguish. Under hypersonic conditions, stronger interactions occur between large vortex structures and boundary layer features, leading to greater vortex deformation. Proper Orthogonal Decomposition (POD) analysis is applied to explore flow dynamics, with the first two spatial modes capturing over 38% of the flow's energy at Mach 5.0. The upper vortex structures exhibit a laminated pattern rather than a uniform flow distribution, indicating a shift in flow characteristics driven by vortex-boundary layer interactions. These findings inform the design of micro-vortex generators for enhanced boundary layer control in hypersonic vehicles, potentially improving aerodynamic stability and reducing thermal loads.

***Keywords*:** LES, hypersonic flow, flow control, vortex structure, POD

Abbreviations

SBLI	Shock-Boundary Layer Interactions
MVG	Micro Vortex Generator
PIV	Particle Image Velocimetry
NPLS	Numerical Particle Laser Scattering
RANS	Reynolds-Averaged Navier-Stokes
LES	Large Eddy Simulation
DNS	Direct Numerical Simulation
WENO	Weighted Essentially Non-Oscillatory
POD	Proper Orthogonal Decomposition
PCA	Principal Component Analysis

DOI: https://doi.org/10.37256/est.6220257062

1. Introduction

Shock-Boundary Layer Interactions (SBLI) in high-velocity flows pose significant challenges to the integrity of the flow field, often resulting in considerable flow separation. This separation can lead to flow instability and a notable reduction in total pressure, which in turn adversely impacts the operational efficiency and overall propulsive performance of propulsion systems in high-speed vehicles [1]-[3]. The implications of these interactions are critical, as they can compromise the aerodynamic performance and maneuverability of advanced aerospace vehicles, necessitating effective mitigation strategies.

Micro Vortex Generators (MVGs) have emerged as a validated and innovative solution to counteract the negative effects of SBLI [4]-[7]. These compact devices, typically smaller than the thickness of the boundary layer, can be seamlessly integrated into the boundary layer itself. This integration minimizes parasitic drag compared to traditional full-scale vortex generators, making MVGs an attractive option for enhancing aerodynamic performance. Engineered specifically to modify flow characteristics, MVGs create unique flow structures that disrupt unfavorable pressure gradients caused by shock waves. This disruption promotes better boundary layer attachment and delays flow separation, which are crucial for maintaining optimal aerodynamic conditions. However, at higher Mach numbers, these structures generated by MVG can become unstable or dissipate more quickly due to increased compressibility effects [8].

Current research is focused on optimizing MVG configurations to intentionally disrupt wake flows, thereby enhancing mixing and improving the health of the boundary layer. This line of inquiry not only advances the design and functionality of individual MVGs but also contributes to a broader understanding of SBLI phenomena in high-speed flows. Over the last decade, both experimental and computational studies have been conducted to explore the efficacy of MVGs. For instance, Babinsky et al. [5] executed a series of experiments employing various MVG designs and thoroughly investigated their control effects. Sun et al. [9] utilized Particle Image Velocimetry (PIV) to analyze the three-dimensional instantaneous flow organization downstream of a micro-ramp within a supersonic boundary layer. Similarly, Wang et al. [10] conducted Numerical Particle Laser Scattering (NPLS) and PIV experiments in a low-noise supersonic wind tunnel to gain insights into the flow dynamics.

Numerical simulations have played a vital role in comparative analyses and subsequent design optimizations of MVGs. These simulations have employed various methodologies, including Reynolds-Averaged Navier-Stokes (RANS), hybrid RANS/Large Eddy Simulation (LES), and monotone integrated LES techniques. Rizzetta and Visbal [11] utilized implicit LES with a high-order approach to simulate the flow field over a compression corner, while von Kaenal et al. [12] applied an approximate de-convolution model for LES on ramp flow. In our previous investigations, we executed numerical simulations of supersonic ramp flow incorporating MVG control at a Mach number of 2.5 and a Reynolds number of 5,760. These simulations were aimed at elucidating the complex flow structures, particularly the three-dimensional vortex formations in the vicinity of the MVG.

Our meticulous analysis [13]-[15] of the flow field surrounding the MVG and its adjacent regions has led to the proposal of a dynamic vortex model. The results from our Large Eddy Simulations (LES) revealed the presence of a series of ring-like (or Ω-shaped) vortices generated downstream of the MVG, which propagate further along the flow. Notably, we observed a significant reduction in the intensity of shock waves at the ramp corner, attributed to the influence of the boundary layer enriched with these ring-like vortices [16]. This finding underscores the potential of MVGs in mitigating shock wave impacts and enhancing boundary layer performance.

Ongoing studies are further exploring these dynamics, with an emphasis on the sensitivity of vortex behavior to variations in the Mach number. Understanding these sensitivities is crucial for informing aerodynamic design and flow control strategies aimed at optimizing performance within supersonic boundary layers. The remainder of this manuscript is organized as follows: section 2 provides a concise introduction to the numerical methodologies employed; section 3 presents our findings; section 4 discusses the implications of these findings; and section 5 concludes with a summary of the current study.

2. Numerical methods

To elucidate the underlying mechanisms and attain a comprehensive understanding of the dynamics of MVG, the implementation of high-order Direct Numerical Simulation (DNS) and LES is imperative. Our LES approach employed

the unfiltered variant of the Navier-Stokes equations, utilizing a fifth-order bandwidth-optimized Weighted Essentially Non-Oscillatory (WENO) scheme [17] at Mach numbers of 2.5 and 5 with a Reynolds number of 5,760.

The governing equations are articulated in the non-dimensional form of the Navier-Stokes equations, presented in conservative formulation as delineated below:

$$\frac{\partial Q}{\partial t}+\frac{\partial F}{\partial x}+\frac{\partial G}{\partial y}+\frac{\partial H}{\partial z}=\frac{1}{Re}\left(\frac{\partial F_v}{\partial x}+\frac{\partial G_v}{\partial y}+\frac{\partial H_v}{\partial z}\right), \tag{1}$$

where the vector of conserved quantities Q, inviscid flux vector E, F, and G, and viscous flux vector E_v, F_v, and G_v are

$$Q=\left[\rho,\ \rho u,\ \rho v,\ \rho w,\ e\right]^T,\ F=\left[\rho u,\ \rho u^2+p,\ \rho uv,\ \rho uw,\ (e+p)u\right]^T,$$

$$G=\left[\rho v,\ \rho uv,\ \rho v^2+p,\ \rho vw,\ (e+p)v\right]^T,\ H=\left[\rho w,\ \rho uw,\ \rho vw,\ \rho w^2+p,\ (e+p)w\right]^T, \tag{2}$$

$$F_v=\left[0,\ \sigma_{xx},\ \sigma_{xy},\ \sigma_{xz},\ u\sigma_{xx}+v\sigma_{xy}+w\sigma_{xz}+\frac{1}{(\gamma-1)\mathrm{PrM}_\infty^2}k(T)\frac{\partial T}{\partial x}\right]^T, \tag{3}$$

$$G_v=\left[0,\ \sigma_{xy},\ \sigma_{yy},\ \sigma_{yz},\ u\sigma_{xy}+v\sigma_{yy}+w\sigma_{yz}+\frac{1}{(\gamma-1)\mathrm{PrM}_\infty^2}k(T)\frac{\partial T}{\partial y}\right]^T, \tag{4}$$

$$H_v=\left[0,\ \sigma_{xz},\ \sigma_{yz},\ \sigma_{zz},\ u\sigma_{xz}+v\sigma_{yz}+w\sigma_{zz}+\frac{1}{(\gamma-1)\mathrm{PrM}_\infty^2}k(T)\frac{\partial T}{\partial z}\right]^T. \tag{5}$$

The components of viscous stress are

$$\sigma_{xx}=\frac{2}{3}\mu(T)\left(2\frac{\partial u}{\partial x}-\frac{\partial v}{\partial y}-\frac{\partial w}{\partial z}\right),\ \sigma_{yy}=\frac{2}{3}\mu(T)\left(-\frac{\partial u}{\partial x}+2\frac{\partial v}{\partial y}-\frac{\partial w}{\partial z}\right),$$

$$\sigma_{zz}=\frac{2}{3}\mu(T)\left(-\frac{\partial u}{\partial x}-\frac{\partial v}{\partial y}+2\frac{\partial w}{\partial z}\right),\ \sigma_{xy}=\mu(T)\left(\frac{\partial u}{\partial y}+\frac{\partial v}{\partial x}\right), \tag{6}$$

$$\sigma_{xz}=\mu(T)\left(\frac{\partial u}{\partial z}+\frac{\partial w}{\partial x}\right),\ \sigma_{yz}=\mu(T)\left(\frac{\partial w}{\partial y}+\frac{\partial v}{\partial z}\right).$$

In order to solve the flow field with complex boundary (wall boundary with MVG), we use the governing equations in curvilinear coordinates [18],

$$\frac{\partial \hat{Q}}{\partial t}+\frac{\partial \hat{F}}{\partial \xi}+\frac{\partial \hat{G}}{\partial \eta}+\frac{\partial \hat{H}}{\partial \zeta}=\frac{1}{Re}\left(\frac{\partial \hat{F}_v}{\partial \xi}+\frac{\partial \hat{G}_v}{\partial \eta}+\frac{\partial \hat{H}_v}{\partial \zeta}\right), \tag{7}$$

where

$$\hat{Q}=\frac{Q}{J},\ \hat{F}=\frac{\xi_x F+\xi_y G+\xi_z H}{J},\ \hat{G}=\frac{\eta_x F+\eta_y G+\eta_z H}{J},\ \hat{H}=\frac{\zeta_x F+\zeta_y G+\zeta_z H}{J},$$

$$\hat{F}_v = \frac{\xi_x F_v + \xi_y G_v + \xi_z H_v}{J},\ \hat{G}_v = \frac{\eta_x F_v + \eta_y G_v + \eta_z H_v}{J},\ \hat{H}_v = \frac{\zeta_x F_v + \zeta_y G_v + \zeta_z H_v}{J}. \tag{8}$$

J is the coordinate transformation matrix between the curvilinear (ξ, η, ζ) and Cartesian (x, y, z) coordinate systems.

The reference values for length, density, velocity, temperature and pressure are δ_{in}, ρ_∞, U_∞, T_∞, and $\rho_\infty U_\infty^2$ respectively, where δ_{in} is the inflow displacement thickness. And the Mach number M_∞ and Reynolds number Re are expressed as

$$M_\infty = \frac{U_\infty}{\sqrt{\gamma R T_\infty}},\ Re = \frac{\rho_\infty U_\infty \delta_{in}}{\mu_\infty}, \tag{9}$$

where R is the ideal gas constant, γ the ratio of specific heats and μ_∞ the viscosity.

The spatial domain concerning the fluid dynamics in conjunction with the MVG is illustrated in Figure 1. The grid number for the whole system is $n_{\text{spanwise}} \times n_{\text{normal}} \times n_{\text{streamwise}} = 137 \times 192 \times 1{,}600$.

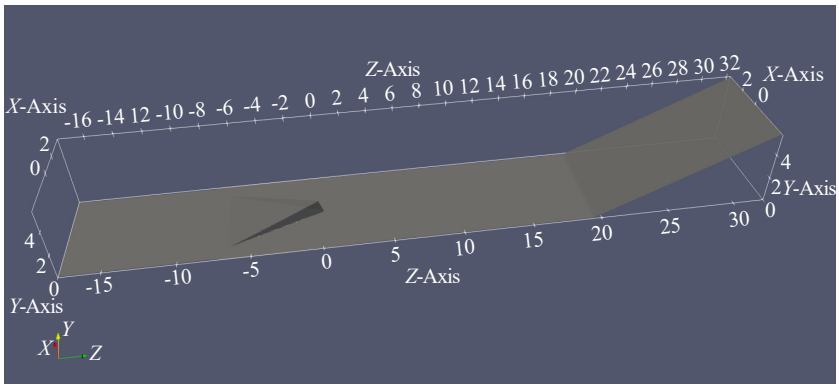

Figure 1. The schematic of the flow domain

The conditions of adiabaticity, along with a zero-gradient pressure condition and non-slip conditions, are implemented at the wall surfaces. In order to mitigate the potential for wave reflection, non-reflective boundary conditions are employed at the upper boundary. The boundary conditions applicable to both the frontal and dorsal boundary surfaces in the spanwise direction are managed as periodic conditions. The outflow boundary conditions are delineated as a characteristic-based condition, facilitating the management of outgoing flows without inducing reflections. To fabricate a genuine turbulent inlet, turbulent flow profiles derived from prior Direct Numerical Simulations (DNS) are utilized as the time-variant inflow [19]. Following a brief development phase, the inflows produced upstream of the MVG evolve into fully developed turbulent flows. The detailed numerical methods and schemes used in this study can be found in [20].

3. Numerical results and comparison

To visualize the vortical structures, a novel vortex identification method, Liutex [21], which can capture both axes and the magnitude of local fluid rotation, is used in this study. Liutex uses RS decomposition to separate non-dissipative rigid rotation from dissipative shear shown as,

$$\omega = R + S \tag{10}$$

$$R = \left[(\omega \cdot r) - \sqrt{(\omega \cdot r)^2 - 4\lambda_{ci}^2} \right] r \tag{11}$$

where r is the real eigenvector of ∇v and $\omega \cdot r$.

Figure 2 illustrates the vortex formations induced behind the MVG at Mach number 2.5 (Figure 2a) and Mach number 5.0 (Figure 2b), respectively, employing Liutex iso-surfaces for visualization. In both scenarios examined, we observe the emergence of analogous flow separations originating from the lateral sides of the MVG and extending towards the posterior region of the MVG.

At a Mach number of 2.5, the vortex configurations display a notable degree of regularity, particularly within the upper ring-like vortices. These vortices maintain a coherent structure, indicative of a more regular flow regime that allows for clearer delineation of vortex boundaries.

In stark contrast, when the flow reaches a Mach number of 5.0, the behavior of the vortex formations becomes significantly more intricate and chaotic. While ring-like vortices are still present, they are characterized by pronounced distortion and a lack of well-defined edges. This complexity suggests a transition to a more turbulent flow state, where interactions among the vortices lead to a greater variety of shapes and sizes, complicating the overall flow dynamics. The increased Mach number not only affects the stability of the vortices but also enhances the influence of compressibility effects, further contributing to the intricate patterns observed in the vortex structures at this higher speed.

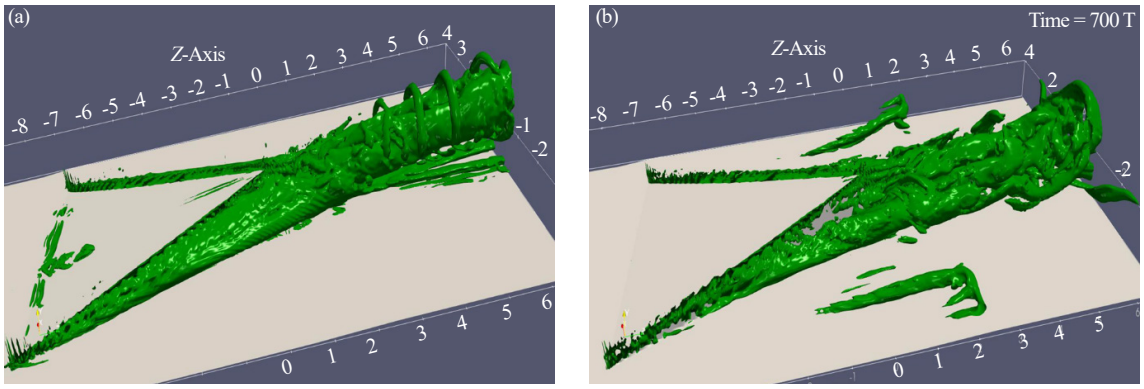

Figure 2. Iso-surface of $||R||$ = 0.3. (a) Mach number Ma = 2.5; (b) Mach number Ma = 5.0

Figure 3 presents a detailed illustration of the spanwise vorticity distribution observed on the central spanwise plane for two distinct cases. The visualization prominently highlights the velocity shear layer that emerges downstream of the MVG, a critical feature in understanding flow behavior.

In the scenario characterized by a Mach number of 2.5, the flow dynamics exhibit a notable trend: the boundary layer is comparatively thinner due to the increased flow rates. This results in a reduced height of the momentum deficit that is generated in the wake of the MVG. The entire flow field structure experiences a rapid ascent, and with the exception of the immediate vicinity surrounding the MVG, there is a pronounced lack of interaction with the underlying region of the boundary layer. This suggests a more streamlined flow pattern, where the influence of the MVG is largely confined to its immediate surroundings.

In contrast, the scenario at a Mach number of 5.0 reveals a markedly different flow behavior. Here, interactions between the flow above and below the boundary layer become significantly more pronounced. The presence of these interactions indicates that the structures formed within the boundary layer are likely influenced by the dynamics occurring at the lower regions. This complexity at higher Mach numbers underscores the intricate nature of the flow dynamics, where the interactions between the upper and lower sections of the boundary layer lead to a richer and more nuanced flow structure. The implications of these findings are crucial for understanding the behavior of high-speed flows and the effectiveness of MVGs in manipulating such flows.

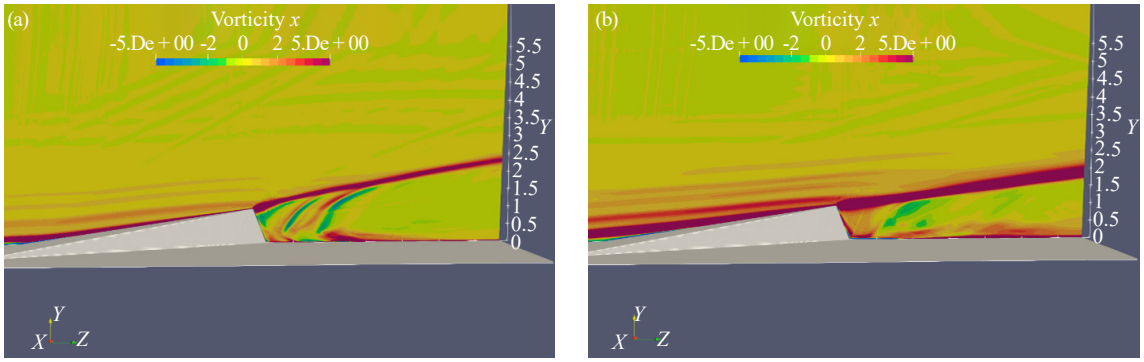

Figure 3. Spanwise vorticity distribution on the central spanwise plane (x = 0). (a) Mach number Ma = 2.5; (b) Mach number Ma = 5.0

Figure 4 depicts the time-averaged three-dimensional momentum deficits noted downstream of the MVG for two separate scenarios, utilizing the iso-surface of streamwise velocity as a visual aid. In the scenario with a Mach number of 2.5, the formation of ring-like vortices is remarkably evident, resulting in the development of a distinct upper structure. This upper structure is clearly highlighted in the time-averaged data, indicating that the momentum deficit in the Mach 2.5 case is considerably more streamlined and narrower than in the other scenario examined. These results emphasize the significant impact of different vortex structures on the overall flow dynamics, indicating that the unique attributes of the vortices produced at varying Mach numbers are essential in influencing the flow patterns and momentum distribution downstream. The variations seen in momentum deficits not only represent the intricacies of fluid behavior but also underscore the significance of comprehending these dynamics for enhancing aerodynamic designs and boosting performance in high-speed flow scenarios.

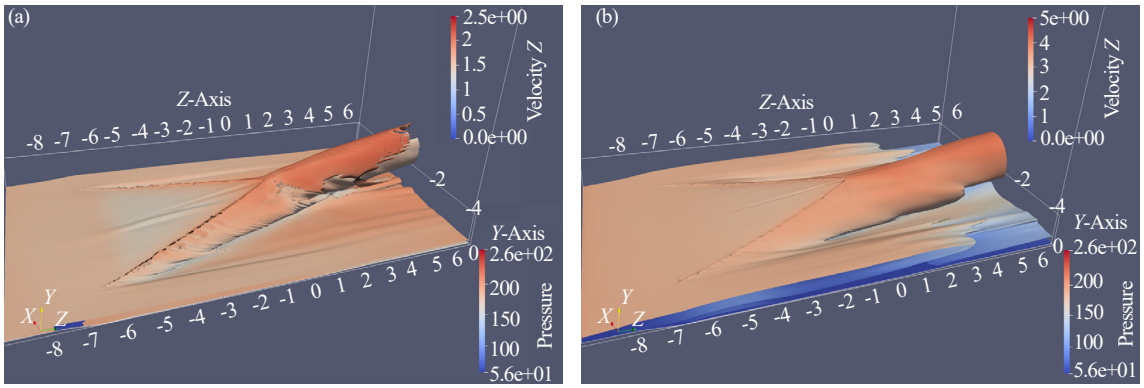

Figure 4. Iso-surface of streamwise velocity at u = 0.5. (a) Mach number Ma = 2.5; (b) Mach number Ma = 5.0

In order to conduct a more in-depth examination of the variations in flow dynamics across different Mach numbers, we scrutinized the velocity distributions along orthogonal lines situated at three discrete positions downstream of the MVG, as illustrated in Figure 5. These orthogonal lines are strategically located at intervals of 2 h, 4 h, and 6 h (where h denotes the height of the MVG) from the trailing edge of the MVG, which correspond to proximal, intermediate, and distal distances, respectively. This analysis facilitates a thorough comprehension of the developmental progression of the flow at various downstream stages from the MVG, thereby elucidating the impact of Mach number on the characteristics of the flow.

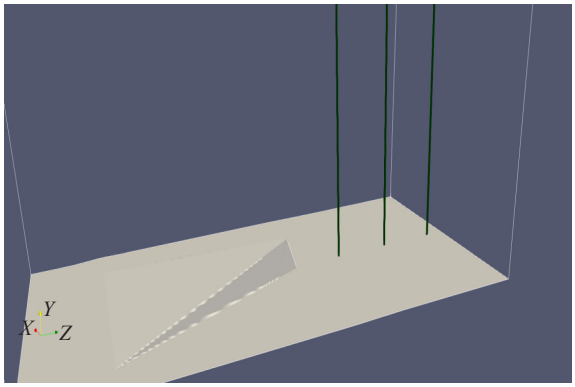

Figure 5. Streamwise positions of the three normal lines selected downstream of MVG

Figure 6 illustrates the velocity profiles along three distinct normal lines located downstream of the MVG. To enable a meaningful comparative analysis, the velocities presented have been normalized by the Mach number. In the case of a Mach number of 2.5, a pronounced and significant reduction in streamwise velocity can be observed within the momentum deficit region. This reduction not only becomes more evident as the flow continues downstream but also indicates a progressive amplification of the velocity deficit. Such behavior suggests that the momentum deficit intensifies with increasing distance from the MVG, although it remains relatively close to the source. Conversely, for the scenario with a Mach number of 5.0, the initial stages exhibit an almost negligible decrease in streamwise velocity. At a distance of z = 4 h from the MVG, the velocity profile within the momentum deficit region appears nearly linear, demonstrating minimal deviation from the baseline. It is only at a further distance, specifically at z = 6 h, that a slight decline in velocity begins to manifest, indicating a delayed onset of momentum deficit development in this higher Mach number scenario. Moreover, the figure indicates that the initial thickness and height of the momentum deficit are relatively similar in both Mach number cases. However, as the flow progresses downstream, the height of the momentum deficit in the Ma = 2.5 scenario gradually increases, reflecting a more pronounced development of the deficit over distance. In contrast, the Ma = 5.0 case exhibits a relatively stable height for the momentum deficit initially, with observable signs of development emerging only at greater downstream positions. This distinction highlights the differing dynamics of momentum deficit evolution influenced by varying Mach numbers.

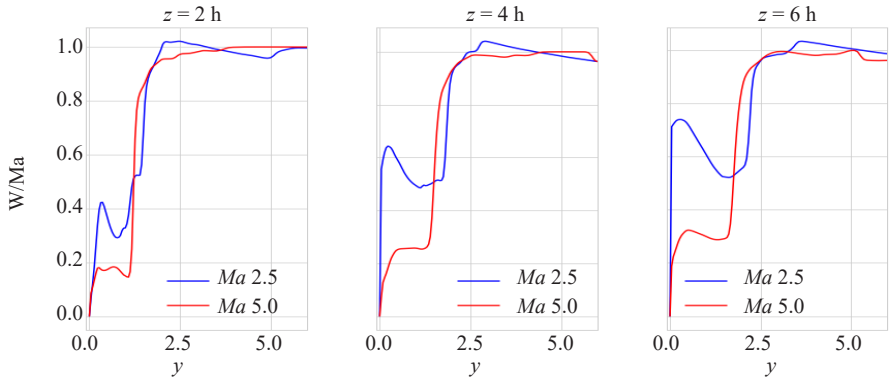

Figure 6. The velocity profiles along the normal lines

Figure 7 provides a detailed visualization of the separation patterns occurring at the wall boundary, employing both streamlines and the normal derivative of the streamwise velocity $\frac{\partial w}{\partial y}$ to illustrate the differences observed in two distinct cases. The dark blue regions depicted behind the MVG, which extend downstream from the MVG's trailing

edge, signify the zones of flow separation along the wall boundary. The separation zone near the MVG tail measures approximately 1.2 at Mach 2.5, increasing to about 2.3 at Mach 5.0. In the scenario characterized by a Mach number of 2.5, these separation zones appear relatively compact and somewhat isolated from one another. This suggests that the influence of the MVG on the surrounding flow is limited, resulting in a more stable flow structure with less pronounced separation effects. Conversely, in the case of a Mach number of 5.0, the separation zones on either side of the MVG tail are markedly larger and exhibit a significant degree of interconnection, as depicted in Figure 7b. This observation points to a more intense flow separation phenomenon at the higher Mach number, indicating a stronger interaction between the boundary layer and the large vortex structures generated by the MVG. The pronounced flow separation observed at Ma = 5.0 not only highlights the increased complexity of the flow dynamics but also suggests a more substantial influence from the lower boundary layer on the development of these large-scale vortex structures. This finding is consistent with the trends illustrated in Figure 3, which documented a heightened interaction between the lower boundary layer and the coherent vortex formations at elevated Mach numbers. The enhanced flow separation at Ma = 5.0 serves to underscore the intricate interplay between the boundary layer and the overall flow structure, revealing how variations in Mach number can significantly alter the flow characteristics and the effectiveness of devices like the MVG in manipulating airflow.

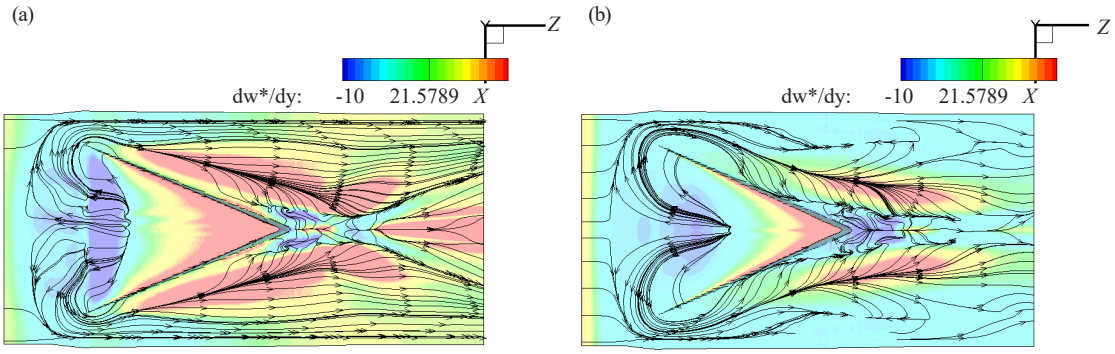

Figure 7. Streamlines and the normal derivative of streamwise velocity $\frac{\partial w}{\partial y}$ at the wall boundary: (a) Mach number Ma = 2.5; (b) Mach number Ma = 5.0

Figure 8 illustrates the distribution of streamwise vorticity across three distinct cross-sections located downstream of the MVG, specifically at the spatial coordinates z = 2 h, 4 h, and 6 h. The prominent blue and red regions observed in the upper sections of these cross-sections are indicative of the presence of counter-rotating streamwise vortices that reside within the momentum deficit zone. These vortices are integral to understanding the flow structure that is significantly altered by the influence of the MVG. In the scenario characterized by a Mach number of 5.0, a noteworthy observation is made regarding the positioning of these streamwise vortices, which are found to be situated at a lower elevation compared to their counterparts in the Mach 2.5 case. This downward shift in the vortices' location leads to a marked increase in their interaction with the structures present in the lower boundary layer, as previously highlighted in Figures 3 and 7. The enhanced interaction, as depicted in Figure 8b, implies that at elevated Mach numbers, the flow dynamics exhibit heightened complexity. This complexity arises from the significant influence exerted by the lower boundary layer on the overall vortex structure, suggesting a more intricate interplay between the vortices and the surrounding flow environment.

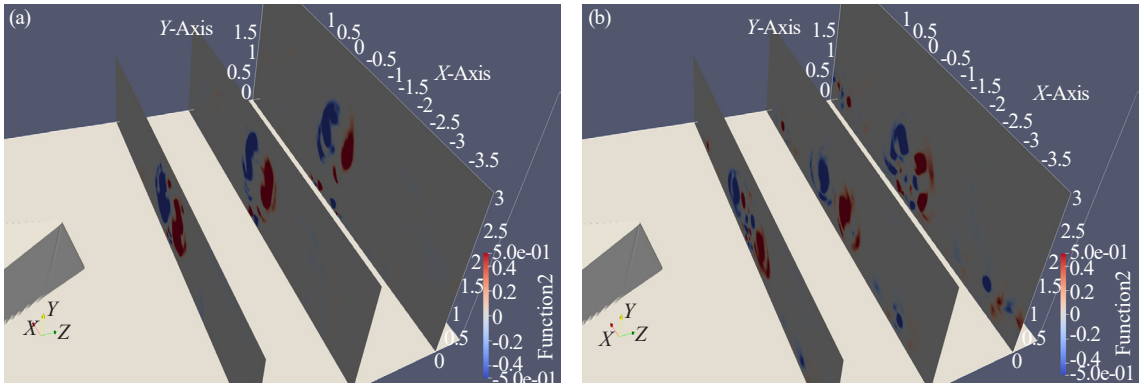

Figure 8. Streamwise vorticity distribution on three cross sections in the downstream of MVG (z = 2 h, 4 h and 6 h respectively). (a) Mach number Ma = 2.5; (b) Mach number Ma = 5.0

Figure 9 illustrates the distribution of normal velocity components observed on the central streamwise plane for two distinct cases downstream of the MVG. Within this region, a pair of counter-rotating streamwise vortices emerges, which are instrumental in creating a momentum deficit. This phenomenon leads to a significant up-washing effect on the central plane, resulting in the formation of pronounced high normal velocity zones depicted in the figure. The up-washing effect is particularly noteworthy as it not only elevates the high-speed fluid but also causes the low-speed (streamwise) fluid to be lifted upwards. This upward movement contributes to the development of a momentum deficit, which is responsible for the formation of a shear layer, as illustrated in Figure 3. A closer examination of Figure 9 reveals a marked difference in the intensity of the upwash effect between the two cases. Specifically, the upwash effect observed in the Mach 2.5 scenario is significantly more pronounced than that in the Mach 5.0 case. This disparity suggests that variations in Mach number can substantially influence the dynamics of fluid flow, particularly in relation to the strength of the vortices and their associated effects on velocity distribution in the wake of the MVG.

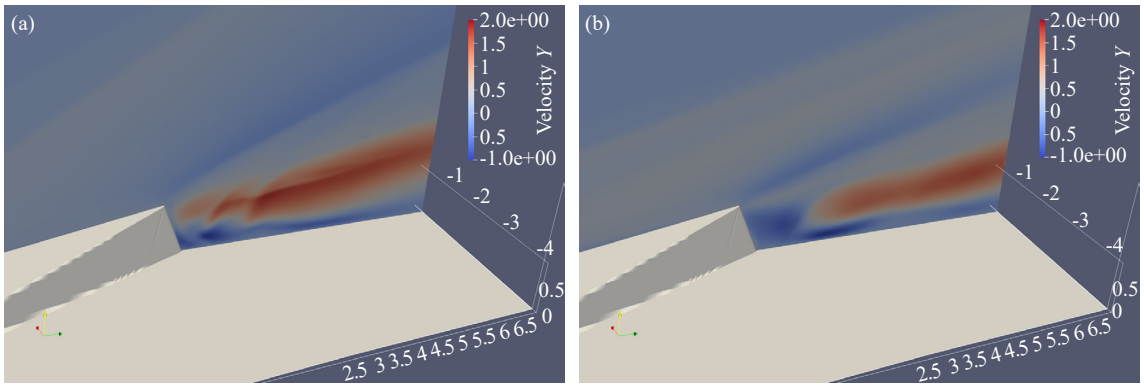

Figure 9. Distribution of the normal velocity component (v) on the central streamwise plane (x = 0) behind the MVG. (a) Mach number Ma = 2.5; (b) Mach number Ma = 5.0

To better illustrate the differences in vortex structures between the two cases, Figure 10 displays the Liutex iso-surface contoured by streamwise velocity. In the Mach 2.5 case (Figure 10a), prominent red ring-like vortices are clearly visible and far more pronounced than those in the Mach 5.0 case. Additionally, the inner pair of streamwise vortices in Mach 2.5 exhibits slightly higher velocities, indicating a more energetic and stable flow regime compared to the more complex structure seen at Mach 5.0.

At Mach 5.0, spiral-shaped streamwise vortices develop on either side of the structure behind the MVG, likely influenced by the outer separation zones flanking it. As the flow moves downstream, these vortices interact with the

down-sweep effect at the outer edge of the momentum deficit, altering their topology and contributing to a broader vortex structure, unlike the more compact formations in the Mach 2.5 scenario.

To delve deeper into the intricate differences in flow structures between these two cases, we will employ Proper Orthogonal Decomposition (POD) in the subsequent section to analyze the vortex dynamics in greater detail.

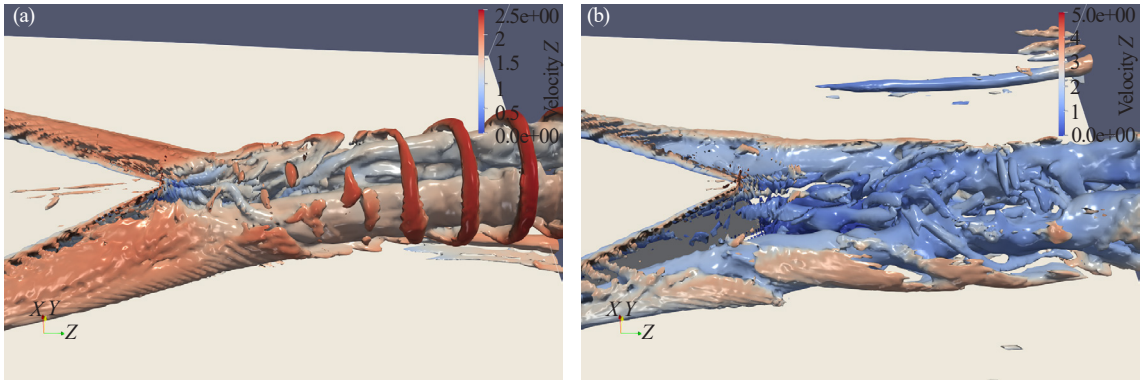

Figure 10. Iso-surface of $||R||$ = 0.3, contoured by streamwise velocity. (a) Mach number Ma = 2.5; (b) Mach number Ma = 5.0

4. POD analysis

The Proper Orthogonal Decomposition (POD) method [22] constitutes a robust technique akin to Principal Component Analysis (PCA) within the domain of fluid mechanics, facilitating the analysis and simplification of intricate flow fields. POD serves to discern the most critical dynamic structures within a flow by partitioning numerical results (e.g., velocity or pressure fields) across various temporal instances into orthogonal modes pertaining to both spatial and temporal dimensions. This methodology proves particularly advantageous for elucidating complex structures within a flow field by examining the predominant modes to encapsulate the principal characteristics of the flow, thereby establishing its efficacy as a valuable instrument for both steady-state and transient simulations. Its application spans a diverse array of engineering challenges, encompassing vortex dynamics, flow control, and optimization studies. This technique necessitates the resolution of the eigenvalue problem associated with the autocorrelation matrix derived from a snapshot of the flow field, which yields a set of orthogonal basis functions that accurately represent the prevailing structures within the flow. In the present investigation, the vortex-based POD (utilizing Liutex in lieu of velocity profiles) is employed to gain insights into the intricate vortex structures. Numerical flow fields encompassing 20,000 timesteps were utilized (enough for the free stream to flow through the entire flow field 100 times in Mach 2.5).

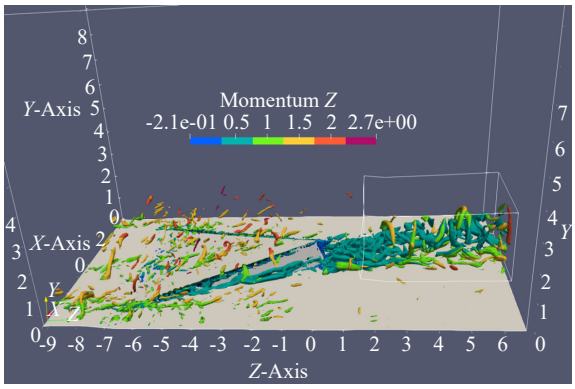

Figure 11. Illustration of the subdomain selected for the POD analysis

Figure 11 illustrates the subdomain employed in POD analysis. The region spans approximately 6 h in the streamwise direction and rises to a height of about 4 h. Although the subdomain is significantly smaller than the full domain, it effectively captures the area influenced by the vortex structures generated by the MVG. The lower viscous sublayer is omitted, and our POD analysis is exclusively concentrated on the more substantial coherent structures.

Figure 12 presents an illustration of the POD analysis. The physical field, specifically the Liutex vector field utilized in this investigation, can be organized into a column vector for each discrete time interval, commonly referred to as a snapshot. Consequently, the complete dataset of numerical solutions across various time steps can be constructed into an extensive snapshot matrix. Through the computation of the associated covariance matrix, one can derive the eigenvalues, which represent the energy associated with the modes, in addition to identifying the prevalent spatial modes and temporal modes (time coefficients).

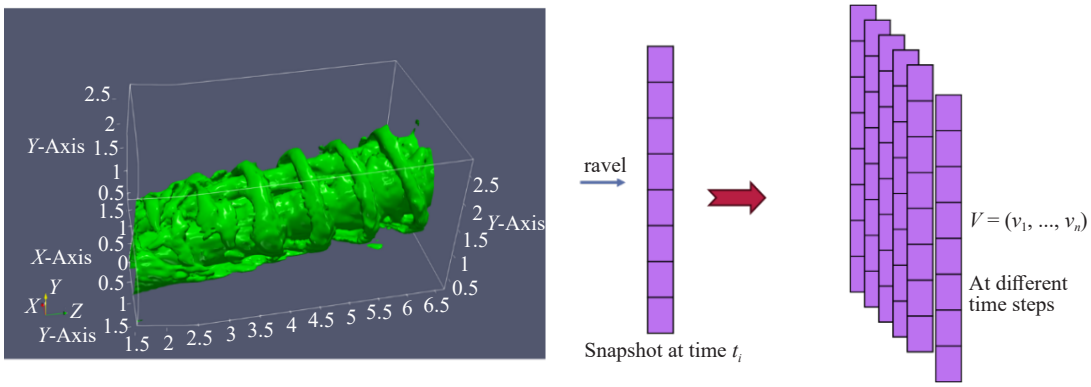

Figure 12. Illustration of the POD analysis

Figure 13a illustrates the energy distribution across the various POD modes, while Figure 13b presents the cumulative energy associated with these modes. In both visual representations, it is evident that the first three modes play a pivotal role in driving the evolution of the system, collectively accounting for a significant portion of the energy dynamics. Notably, the first six modes together contribute to over 60% of the total energy, underscoring their importance in the overall behavior of the system. Interestingly, while the first three modes exhibit a clear dominance, the energy distribution among the third, fourth, and fifth modes reveals some substantial variations, indicating a more complex interplay among these specific modes. In contrast, the remaining modes exhibit a relatively uniform energy distribution, suggesting that they contribute less significantly to the system's dynamics.

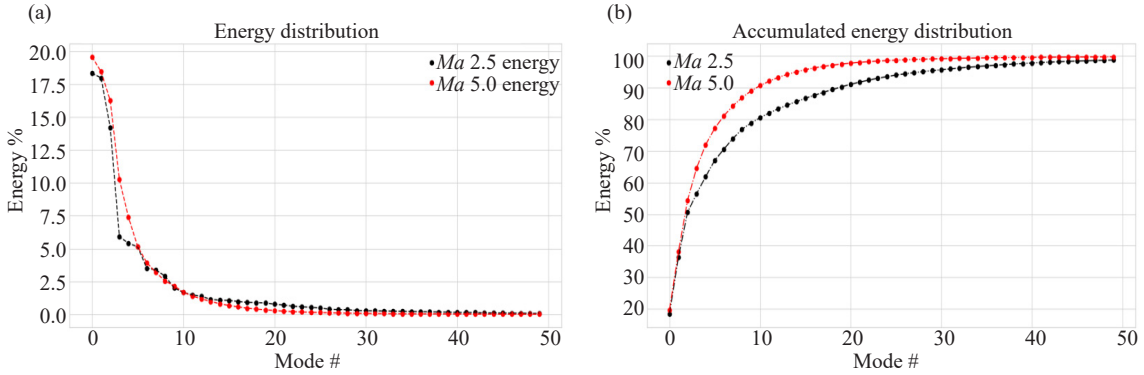

Figure 13. POD modes energy distribution. (a) energy of each mode; (b) accumulated energy

Figure 14 illustrates the initial six modes for both conditions, emphasizing both commonalities and divergences. In both conditions, the predominant modes are characterized by spanwise rotating vortex configurations within the upper stratum. In the scenario of Mach 2.5, these vortices demonstrate a systematic, ring-like arrangement, signifying a more structured flow pattern. In contrast, the Mach 5.0 scenario showcases vortices with irregular geometries, implying a more intricate flow architecture. Moreover, the modes associated with the Mach 5.0 case exhibit a laminated organization rather than a consistent distribution along the flow axis, denoting layers of vortices arranged in a stacked manner. This stands in stark contrast to the homogeneous distribution observed in the Mach 2.5 case. Importantly, the Mach 5.0 scenario is devoid of a streamwise mode analogous to the third mode identified in the Mach 2.5 case, underscoring substantial disparities in the flow dynamics between the two Mach numbers.

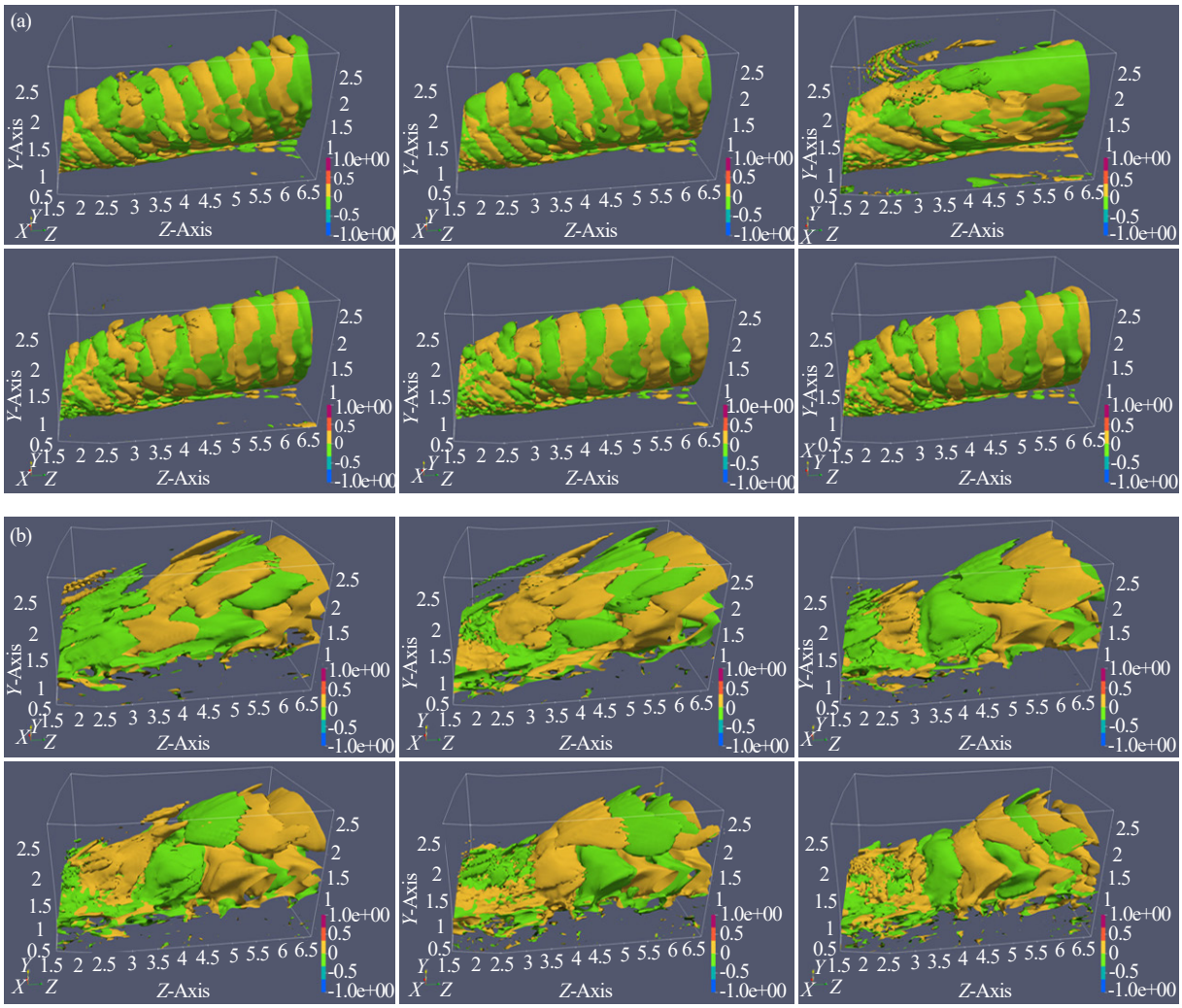

Figure 14. Iso-surface of Liutex for the first 6 POD spatial modes (a) Mach number Ma = 2.5; (b) Mach number Ma = 5.0

Figure 15 illustrates the spectral characteristics of the temporal coefficient corresponding to the initial mode. By examining this spectral distribution, one can identify parallels in both the frequency distribution and the associated power (amplitude). Furthermore, both scenarios indicate that the first mode significantly influences the structural dynamics at a comparable elevated frequency. In conclusion, the results of the POD analysis reveal that, although the flow at Mach number 5.0 undergoes heightened interactions with the underlying structure, resulting in more erratic spatial modes, the overarching structural behavior and its temporal evolution exhibit notable similarities when juxtaposed with the flow at Mach number 2.5.

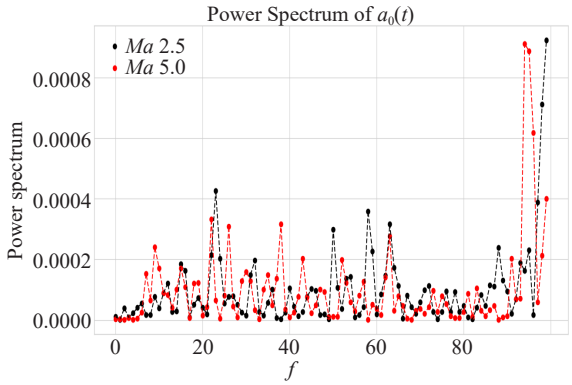

Figure 15. Power spectrum of the time coefficients of the first POD mode

5. Conclusions

In this study, we delve into LES for MVG controlled supersonic and hypersonic flows, specifically focusing on Mach numbers of 2.5 and 5.0. The primary objective is to elucidate the influence of the MVG on the high-speed flow field, with particular attention to the vortex structures that emerge downstream of the MVG. Additionally, a comparative analysis with the results obtained from a lower Mach number case of 2.5 is presented to highlight the variations in flow characteristics across different regimes. Our findings reveal that as the Mach number increases, the detection of ring-like vortices becomes increasingly challenging. This is attributed to the altered flow dynamics at higher speeds, which significantly affect the vortex structures. Notably, the upper flow structures at Mach 5.0 differ markedly from those observed at Mach 2.5, exhibiting a reduction in the regularity and prevalence of ring-like vortices. Contrary to what might be expected, the escalation of the Mach number does not correlate with a more pronounced up-washing effect, suggesting a complex interplay of aerodynamic forces at play. Furthermore, due to the MVG's lower positioning, there is a notable increase in the interaction between the ring-like vortices and the lower vortex structures present within the boundary layer. This interaction leads to a pronounced deformation of the main streamwise vortices, indicating that the flow behavior is highly sensitive to the geometric configuration of the MVG. As the Mach number rises, we observe an expansion of the backflow zone behind the MVG, accompanied by a more pronounced flow separation phenomenon. This separation is indicative of the intricate flow patterns that develop at hypersonic speeds, which can significantly impact the performance and stability of aerodynamic surfaces. To gain deeper insights into the dynamics of the vortex structures, a vortex-based POD analysis was conducted. This analysis revealed the disturbance modes associated with the evolution of the vortex structures, uncovering coherent structures akin to the ring-like vortex modes identified in the Mach 2.5 case. Similar coherent modes with varying frequencies were also detected at Mach 5.0, underscoring the persistence of these structures across different flow regimes. However, a key distinction emerges in the upper structures of these modes at Mach 5.0, which display a laminated configuration rather than a uniform distribution along the flow direction. In order to gain a deeper understanding of the MVG-controlled hypersonic flows and the characteristics of the related vortex structures and their evolution processes, more numerical simulations and experiments at different Mach numbers need to be conducted.

Data availability statement

Data is contained within the article.

Conflicts of interest

The authors declare no conflicts of interest.

References

[1] J. C. Lin, "Review of research on low-profile vortex generators to control boundary-layer separation," *Progress in Aerospace Sciences*, vol. 38, no. 4-5, pp. 389-420, 2002.

[2] P. R. Ashill, J. L. Fulker, and K. C. Hackett, "A review of recent developments in flow control," *The Aeronautical Journal*, vol. 109, no. 1095, pp. 205-232, 2005.

[3] J. P. Dussauge, P. Dupont, and J. F. Debiève, "Unsteadiness in shock wave boundary layer interactions with separation," *Aerospace Science and Technology*, vol. 10, no. 2, pp. 85-91, 2006.

[4] D. Estruch-Samper, L. Vanstone, R. Hillier, and B. Ganapathisubramani, "Micro vortex generator control of axisymmetric high-speed laminar boundary layer separation," *Shock Waves*, vol. 25, no. 5, pp. 521-533, 2015.

[5] H. Babinsky, Y. Li, and C. W. Pitt Ford, "Microramp control of supersonic oblique shock-wave/boundary-layer interactions," *AIAA Journal*, vol. 47, no. 3, pp. 668-675, 2009.

[6] B. Zhang, Q. Zhao, X. Xiang, and J. Xu, "An improved micro-vortex generator in supersonic flows," *Aerospace Science and Technology*, vol. 47, pp. 210-215, 2015.

[7] M. R. Saad, H. Zare-Behtash, A. Che-Idris, and K. Kontis, "Micro-ramps for hypersonic flow control," *Micromachines*, vol. 3, no. 2, pp. 364-378, 2012.

[8] F. Lu, Q. Li, Y. Shih, A. Pierce, and C. Liu, "Review of micro vortex generators in high-speed flow," in 49th AIAA Aerospace Sciences Meeting Including the New Horizons Forum and Aerospace Exposition, 2011.

[9] Z. Sun, F. Scarano, B. W. van Oudheusden, F. F. J. Schrijer, Y. Yan, and C. Liu, "Numerical and experimental investigations of the supersonic microramp wake," *AIAA Journal*, vol. 52, no. 7, pp. 1518-1527, 2014.

[10] B. Wang, W. Liu, Y. Zhao, X. Fan, and C. Wang, "Experimental investigation of the micro-ramp based shock wave and turbulent boundary layer interaction control," *Physics of Fluids*, vol. 24, no. 5, pp. 055110, 2012.

[11] D. P. Rizzetta and M. R. Visbal, "Application of large-eddy simulation to supersonic compression ramps," *AIAA Journal*, vol. 40, no. 8, pp. 1574-1581, 2002.

[12] R. V. Kaenel, L. Kleiser, N. A. Adams, and J. B. Vos, "Large-eddy simulation of shock-turbulence interaction," *AIAA Journal*, vol. 42, no. 12, pp. 2516-2528, 2004.

[13] Y. Yan, Q. Li, C. Liu, A. Pierce, F. Lu, and P. Lu, "Numerical discovery and experimental confirmation of vortex ring generation by microramp vortex generator," *Applied Mathematical Modelling*, vol. 36, no. 11, pp. 5700-5708, 2012.

[14] Y. Yan and C. Liu, "Study on the initial evolution of ring-like vortices generated by MVG," *CEAS Aeronautical Journal*, vol. 4, pp. 433-442, 2013.

[15] Y. Yan and C. Liu, "Shear layer stability analysis in later boundary layer transition and MVG controlled flow," in Proceedings of the 51st AIAA Aerospace Sciences Meeting including the New Horizons Forum and Aerospace Exposition, 2013, pp. 7863-7874.

[16] Y. Yan, C. Chen, P. Lu, and C. Liu, "Study on shock wave-vortex ring interaction by the micro vortex generator controlled ramp flow with turbulent inflow," *Aerospace Science and Technology*, vol. 30, no. 1, pp. 226-231, 2013.

[17] Y. Yan, Y. Yang, S. Yuan, and C. Chen, "Enhancing accuracy in numerical simulations for high-speed flows: Integrating high-order corrections with weighted essentially non-oscillatory flux," *Processes*, vol. 12, no. 4, pp. 642, 2024.

[18] H. Yang, S. Habchi, and A. Przekwas, "General strong conservation formulation of Navier-Stokes equations in nonorthogonal curvilinear coordinates," *AIAA Journal*, vol. 32, no. 5, pp. 936-941, 1994.

[19] Y. Yan, J. Tang, C. Liu, and F. Yang, "DNS study on the formation of lambda rotational core and the role of ts wave in boundary layer transition," *Journal of Turbulence*, vol. 17, no. 6, pp. 572-601, 2016.

[20] Y. Yan, L. Chen, Q. Li, and C. Liu, "Numerical study of micro-ramp vortex generator for supersonic ramp flow control at Mach 2.5," *Shock Waves*, vol. 27, no. 1, pp. 79-96, 2017.

[21] C. Liu, Y. Gao, X. Dong, Y. Wang, J. Liu, Y. Zhang, X. Cai, and N. Gui, "Third generation of vortex identification methods: Omega and Liutex/Rortex based systems," *Journal of Hydrodynamics*, vol. 31, pp. 205-223, 2019.

[22] A. Cammilleri, F. Gueniat, J. Carlier, L. Pastur, E. Memin, F. Lusseyran, and G. Artana, "POD-spectral decomposition for fluid flow analysis and model reduction," *Theoretical and Computational Fluid Dynamics*, vol. 27, pp. 787-815, 2013.